RSC Advances

ROYAL SOCIETY OF CHEMISTRY

www.rsc.org/advances

Cite this: DOI: 10.1039/c0xx00000x

www.rsc.org/xxxxxx

ARTICLE TYPE

Giant Enhancement of Inverted Polymer Solar Cells Efficiency by Manipulating Dual Interlayers with Integrated Approaches

Hsing-Hua Hsieh[a,b], Yun-Ming Sung[a], Fang-Chi Hsu[c,*], Kuo-Jui Hsiao[b], Ya-Ju Lee[b], and Yang-Fang Chen[a,*]

Received (in XXX, XXX) Xth XXXXXXXXX 20XX, Accepted Xth XXXXXXXXX 20XX
DOI: 10.1039/b000000x

Interlayer property is one of the important issues regarding to charge collection efficiency of polymer solar cells. We report a giant enhancement of light harvesting based on the integration of different concepts to manipulate the cathode and anode interlayers in an inverted ITO/ZnO-nanorod/poly(3-hexythiophene):(6,6)-phenyl C_{61} butyric acid methyl ester (P3HT:PCBM)/poly(3,4-ethylenedioxythiophene):poly(styrene sulfonate) (PEDOT:PSS)/Ag cell structure. A layer of conjugated small molecules is self-assembled on the front cathode interlayer while gold nanoparticles are doped into the rear anode interlayer. The former one carries the characteristic of surface passivation and the latter one has the unique property of localized surface plasmon effect. Quite interestingly, both approaches can effectively enhance the exciton dissociation rate and extend the carrier lifetime. Through the integrated approaches in a single cell, by taking the advantage of each individual contribution and the coupling effect between them, the efficiency can be further boosted from 2.02% to 4.36%, which sets the record for the inverted polymer solar cell using ZnO-nanorod as electron transporting layer and P3HT:PCBM as photoactive layer so far.

Introduction

Polymer based bulk heterojunction solar cells have been intensively studied in the past decades due to their potential of developing low cost and scalable renewable energy.[1-3] Tremendous progress has been made in the past few years to improve the device performance and the power conversion efficiency (*PCE*) of the devices has reached 8 – 9%.[4-6] From the practical application perspective, there is still room for further improving their efficiency to compete with their inorganic counterparts.[7-9] It has been shown that an inclusion of cathode (anode) interlayer is also important to elevate cell performance because this interlayer layer can improve the charge collections at electrodes. Materials such as MoO_3, PEDOT:PSS, V_2O_5 and so on have been widely used as the anode interlayer[10-13] while TiO_2, ZnO, water-soluble polymers, small molecules, etc. have been demonstrated to have good electron collection ability.[14-23] Some of those cathode interlayers using organic molecules with designed end groups also show remarkable improvement of open-circuit voltages (V_{oc}).[14-19] Recently, several groups have tried to modify the interlayers by doping metallic nanostructures[24-26] or self-assembling a functional monolayer on the metal-oxide[27-29] to further enhance the device efficiency. It is known that metallic nanostructures, nanoparticles (NPs) for example, can scatter the incident light to extend its optical path within the photoactive layer and the plasmonic near-field from NPs can be coupled into the nearby photoactive materials to expand the cross-section of absorption.[26] This localized surface plasmon resonance (LSPR) effect can be applied either in the front or rear interlayer of the cell, which has been shown to enhance the cell efficiency up to 20% by adopting single type metallic NPs in the front layer.[24-26] Very recently, Yang and co-workers[26] have tried to apply the concept of LSPR effect on both sides of the cell resulting in ~13% increment in *PCE*.

Self-assembling a monolayer on an interlayer is another approach to raise up the cell performance through the mechanisms of enhancing exciton dissociation[30-32], controlling the morphology of the photoactive layer[28,29,33], and improving V_{oc}.[34,35] Each mechanism contributes differently to the cell efficiency ranging from 10% up to 100% of original *PCE*. A monolayer with additional capability of assisting exciton dissociation rate exhibits the highest potential in performance improvement and the application of this concept can be easily carried out in inverted device structure, using the noble metal as the top electrode to collect hole charges. We have previously reported the use of conjugated 2-naphthalenethiol (2-NT) molecule to modify ZnO-nanorod surface and obtained an improved performance of inverted ZnO-nanord/P3HT:PCBM/Ag solar cells[36] for ~ 100%. This conjugated 2-NT molecule has multiple effects on device improvement in the aspects of exciton dissociation rate, cathode interlayer surface passivation, and bulk heterojunction charge transport. The multiple roles of the employed 2-NT monolayer drive the device to keep the best record so far in the presented cell configuration.

Since manipulating the cathode or anode interlayer improves cell performance at different extent, the result infers that it is likely to further enhance the solar cell efficiency if both interlayers are properly treated. It has been shown that the incorporation of metallic NPs into the rear interlayer of the solar cells can achieve a more effective plasmonic scattering than those at the front side because of the reduced optical loss from the destructive interference of scattered light and unscattered light.[26]

Further, the technique of self-assembling is readily to be accomplished on the surface of front interlayer. Thus, considering the fabrication feasibility and performance enhancement factors enable us to drive the best way to achieve the highest efficiency, such as by the integration of LSPR and surface modification effects.

In this contribution, we fabricate inverted solar cells using modified cathode (front) and anode (rear) interlayers through the integrated approaches as described above to sandwich the photoactive layer, poly(3-hexythiophene):(6,6)-phenyl C_{61} butyric acid methyl ester (P3HT:PCBM). A 2-NT monolayer is self-assembled on the ZnO-nanorod array surface, and gold nanoparticles (Au-NPs) embedded PEDOTPSS layer is designed as the rear (anode) interlayer. Generally, NPs of large size (> 50 nm) can cause stronger light scattering, but easily to create shorts in the thin film devices. Thus, we choose Au-NPs of 50 nm in diameter as our scatters in PEDOT:PSS. In contrast to earlier reports adopting LSPR concept in solar cell fabrication, the presented work is the first report to incorporate Au-NPs in the rear interlayer in an inverted device structure. The finished devices are composed of layers of ITO/ZnO-*x*/P3HT:PCBM/PEDOT:PSS:*y*/Ag, where *x* and *y* stand for the modified substances used. Quite interestingly, the integrated manipulation of interlayer treatment can promote the cell efficiency from 2.02% to 4.36% (best cell), approaching 120% increment in *PCE*. This significant enhancement of device efficiency is a result of the combination of several factors including largely improved light absorption efficiency, exciton separation efficiency, and much extended carrier lifetime arising from the joint effects of LSPR and surface modification.

Experimental details

Material preparation

Indium tin oxide (ITO)-coated glass substrates were cleaned by successive sonication in commercial wafer cleaning buffer solution, acetone and isopropanol for 15 min per step and then dried in N_2 gas flow before used. Initially, a 30 nm ZnO film was sputtered onto the ITO-coated glass followed by suspending the substrate in an aqueous solution of 40 mM zinc nitrate (Acros, 98% purity) and 40 mM hexamethylenetetramine (Acros) at 90 °C for 65 min in an oven.[37,38] The well aligned ZnO-nanorod array was then grown and the process was finished by dipping the substrate into deionized water to remove the residual salts and dried in N_2 gas flow. Au-NP suspension with concentration ~ 3.5×10^{10} particles/mL in 0.1 mM citrate buffer was purchased commercially from Aldrich. The average particle size is approximately 50 nm.

Sample fabrication

Inverted solar cells were fabricated on the ZnO-nanorod array substrates before and after surface treatment, respectively. A polymer blend solution composed of 25 mg P3HT (Lumin. Tech. Co.) and 15 mg PCBM (Lumin. Tech. Co.) in 1 mL 1,2-dichlorobenzene (ODCB) was spin-coated onto the ZnO-nanorod arrays to form a photoactive layer at 400 rpm for 40 sec and then dried in air. The resulting film thickness was ~ 200 nm. The PEDOT:PSS:Au solutions were prepared as follows. 50 μL of PEDOT:PSS was diluted in 450 μL of isopropyl alcohol (ref. 39). Au nanoparticle suspension in citrate buffer was vacuum dry to pump out the solvent. The collected Au-NPs from 20, 100, and 200 μL buffer solutions were then added into 500 μL of diluted PEDOT:PSS resulting in a relative Au-NP concentrations of 4, 20, and 40%, respectively. After ultrasonicating for 2 hours, the NP-contained mixtures were then spin-coated onto the P3HT:PCBM layers in the laboratory environment. Finally, a 100 nm thick silver film was thermally deposited on the PEDOT:PSS at pressure around 2×10^{-6} torr to complete the device fabrication. The finished devices were composed of layers of ITO/ZnO-*x*/P3HT:PCBM/PEDOT:PSS:*y*/Ag, where *x* (*y*) can be either none (none) or 2-NT (Au-NPs (Au)). The device with no interlayer treatment; i.e., (*x*, *y*)=(none, none), was chosen as the standard cell. Devices having the rear interlayer doped with Au-NPs of concentration *n*%, the front interlayer modified with 2-NT, and dual interlayers treated with both approaches are denoted as (*x*, *y*) = (none, $Au_{n\%}$), (2-NT, none), and (2-NT, $Au_{n\%}$), respectively. The typical photo-active area defined by the overlapping of the ITO and Ag electrodes for those devices was 5 mm^2. Samples for the optical characterizations were prepared on ITO-coated glass following the same preparation procedures as photovoltaic devices without metal deposition.

Characterization details

The *J*-V characteristics of the finished photovoltaic devices were evaluated by using a Keithley Model 2400 source meter under irradiation intensity of 100 mW/cm^2 from a calibrated solar simulator (Newport Inc.) with AM 1.5G filter. The calibration was done by using a standard Si photodiode. The incident-photon-conversion-efficiency (IPCE) spectra were performed using a setup consisting of a lamp system, a chopper, a monochromator, a lock-in amplifier, and a standard silicon photodetector (ENLI Technology). The UV-visible absorption spectra were measured by using a JASCO Model V-630 UV-vis spectrophotometer. The reflection spectra were collected by using a Lambda Model 850 UV-Vis spectrophotometer. Surface morphologies were obtained by using an atomic force microscopy (AFM, Nanosurf AG., FlexAFM). The open-circuit-voltage-decay measurements were conducted by using a Xenon lamp equipped with a chopper operated at 10 Hz to produce light pulse and the voltage responses of the cells were recorded by an Agilent Model DSO 5052A oscilloscope.

Results and discussion

Fig. 1(a) and (b) display the top-view field emission scanning electron microscopy (FESEM) images for ZnO-nanorod array before and after modified with 2-NT, respectively. The pristine ZnO-nanorods are well oriented along the *c*-axis with well-defined hexagonal end faces of diameters of approximately 50 nm. After modified with 2-NT molecules, there are no noticable changes in the morphology and diameters of those nanorods. Fig. 1(c) shows the extinction spectrum of Au-NPs in adequate solution determined by UV-vis spectroscopy, exhibiting a plasmonic resonance peak located at 530 nm. The average particle size are *ca*. 50±7 nm, estimated from the image of SEM (see inset in Fig. 1(a)). Those Au-NPs are doped into the PEDOT:PSS hole transport layer before contacting with the top Ag electrode. As an example, an illustration for the finished device structure with (*x*, *y*) = (2-NT, Au) is shown in Fig. 1(d).

Fig. 2(a) displays the typical current density(*J*)–voltage(*V*) characteristics of cells doped with various amount of Au-NPs in the rear interlayer and the average performance parameters abstracted over 10 devices are summarized in Table 1. The standard cell denoted as (*x*, *y*) = (none, none) shows the short circuit current density (J_{sc}), open circuit voltage (V_{oc}), fill factor

(*FF*), and power conversion efficiency (*PCE*) of 9.87 ± 0.21 mA/cm^2, 0.50 ± 0.05 V, 41.35 ± 0.71%, and 2.02 ± 0.07%, respectively, which agrees well with that reported in the literature.[40] By doping the rear PEDOT:PSS layer with 4, 20, and 40% of Au-NPs, the performance of the cells improves due to the enhanced J_{sc} and *FF* at different extent and 20% is the optimum concentration for Au-NPs in the structure to achieve the highest *PCE* of the kind. Thus, the rest of the study considers the optimized case of Au-NPs doping.

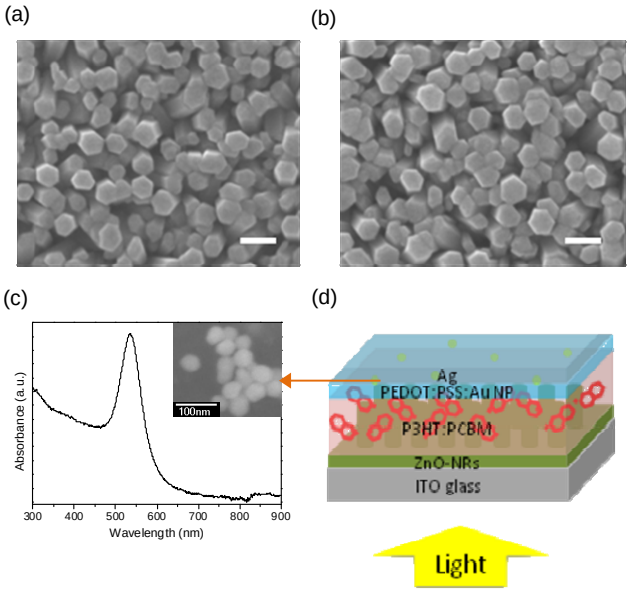

Fig. 1 Top-view FESEM images for (a) pristine and (b) 2-NT modified ZnO-nanorod arrays. Both scale bars stand for 100 nm. (c) UV-vis absorbance for Au-NPs in adequate solution. The inset shows the SEM image of Au-NPs on a silicon wafer. (d) The schematic structure for the cell structure having the front interlayer modified with 2-NT molecules and the rear interlayer doped with Au-NPs.

Fig. 2(b) depicts the comparison of *J*–*V* characteristics for cells with and without interlayer modification and the average performance parameters are also summarized in Table 1. Doping the rear interlayer with 20% Au-NPs results in a moderate improvement in J_{sc} (~8%) and *FF* (~14%) at a constant V_{oc}, and an approximately 21% enhancement in *PCE*. By simply modifying the ZnO-nanorod array with 2-NT molecules, there are ~ 21%, ~24%, ~22%, and ~86% improvement in J_{sc}, V_{oc}, *FF*, and *PCE*, respectively. Apparently, in addition to the much higher J_{sc} and *FF* values than the 20% Au-NP doped case, modifying the front interlayer with 2-NT molecules also enhances V_{oc}. By manipulating both interlayers, the *PCE* of the device is further improved to 4.20 ± 0.10% with a J_{sc}, V_{oc}, and *FF* of 12.76 ± 0.25 mA/cm^2, 0.61 ± 0.05 V, and 53.85 ± 0.70%, respectively. For the best cell, the *PCE* can be up to 4.36%, an improvement factor of ~120%. The largely improved J_{sc}, *FF* and V_{oc} suggest the joint effects of both interlayer treatments.

In order to understand the underlying mechanism of the giant enhancement of the cell efficiency, Fig. 2(c) depicts the recorded IPCE responses in the wavelengths from 350 to 800 nm. It shows a clearly enhancement in IPCE values over the wavelength range from 400 to 600 nm for all modified cells. Fig. 2(d) exhibits the corresponding IPCE enhancement factor with respect to the standard cell. In the wavelengths from 400 to 600 nm, the IPCE enhancement factor is about 1.2 for 2-NT modified device, while it is ~1.1 for Au-NPs doped cells. By combining both approaches, there is approximately 30% increment in the IPCE value, indicating that the collected extra charge is almost the sum of the individual case.

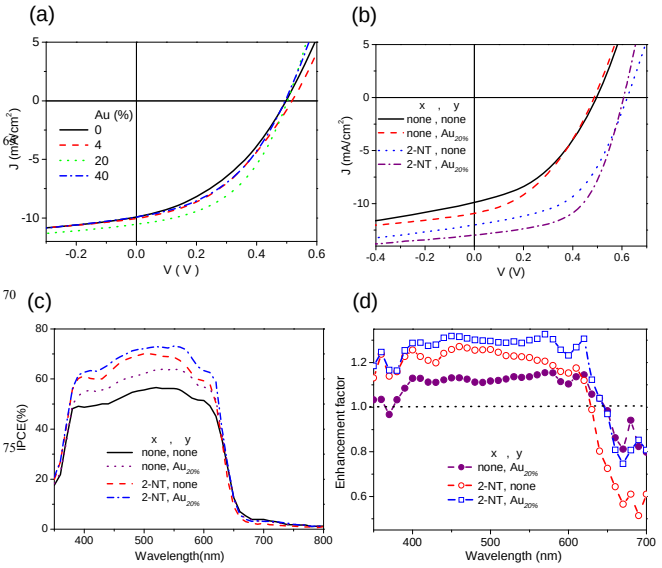

Fig. 2 Evaluation of cell performance. (a) Current density (*J*)-voltage (*V*) characteristics of cells with various Au-NPs concentrations in PEDOT:PSS layer, (b) *J*–*V* characteristics for four types of devices, (c) incident-photon-conversion-efficiency (IPCE) curves, and (d) enhancement factor of IPCE values of the standard and cells under different manipulation conditions.

Fig. 3 depicts the 5 μm × 5 μm morphology images for each layer based on pristine and 2-NT modified ZnO-nanorod arrays obtained by atomic force microscopy (AFM). The root-mean-square (RMS) surface roughnesses for the P3HT:PCBM (Fig. 3(a)), PEDOT:PSS (Fig. 3(c)), and PEDOT:PSS:Au$_{20\%}$ (Fig. 3 (e)) layers based on pristine ZnO-nanorod array are 9.0, 13.4, and 11.2 nm, respectively, while those are 11.9, 8.7, and 10.4 nm, respectively, based on on 2-NT modified one. The surface of the P3HT:PCBM film is slightly rougher on the modified array (Fig. 3(b)) due to the modulation of microscopic mixing result of the photoactive layer by the underneath 2-NT molecules. The subsequently deposited PEDOT:PSS layer is smoother on ZnO-nanorod-2NT/P3HT:PCBM (Fig. 3(d)). However, RMS values for the PEDOT:PSS:Au$_{20\%}$ films on P3HT:PCBM are similar for both pristine and 2-NT modified (Fig. 3 (f)) ZnO-nanorods. It is known that the rougher surface can serve as a template for back reflection contact, which increase light scattering from the top Ag electrode beneficial for improving the phtocurrent. However, the standard device with rougher anode buffer layer shows lower J_{sc} than that doped with Au-NPs, indicating that light scattering due to the Ag back scattering may contribute to the photocurrent, but is not the primary factor for J_{sc} enhancement.

We then measured the UV-vis absorption spectra for the BHJ film under different modification conditions. According to Fig. 4, the structure with neat interlayers shows typical absorption characteristics for P3HT in the wavelengths of 400 – 650 nm with three vibronic state transition peaks at 515, 550, and 600 nm.[41,42] Modifying the front interlayer with 2-NT molecules neither alters the spectra feature nor the photon absorption efficiency. However, incorporating 20% Au NPs into the rear interlayer enhances light absorption of the photoactive film in 450 – 600 nm region. The

Table 1 Performance parameters of solar cells with and without interlayer manipulation under AM 1.5G illumination at 100 mW/cm^2.

(x,y)	J_{sc} (mA/cm^2)	V_{oc} (V)	*FF* (%)	*PCE* (%)	R_s (Ωcm^2)	R_{sh} (Ωcm^2)
(none, none)	9.87±0.21	0.50±0.05	41.35±0.71	2.02±0.07	5.6±0.7	274.6±7.7
(none, $Au_{4\%}$)	10.32±0.20	0.50±0.05	42.74±0.72	2.20±0.11	5.7±0.7	265.3±7.6
(none, $Au_{20\%}$)	10.73±0.28	0.49±0.06	46.98±0.77	2.45±0.13	6.0±0.7	263.7±8.6
(none, $Au_{40\%}$)	10.15±0.30	0.49±0.07	44.04±0.75	2.18±0.17	7.3±0.7	266.6±8.3
(2-NT, none)	12.00±0.22	0.62±0.04	50.29±0.69	3.75±0.06	5.0±0.7	294.4±7.2
(2-NT, $Au_{20\%}$)	12.76±0.25	0.61±0.05	53.85±0.70	4.20±0.10	5.3±0.8	286.5±8.1

average enhancement factor is ~1.05 (see inset in Fig. 4), suggesting a harvest of additional 5% of incident photons by the device structure as 20% Au-NPs is added. Because Au-NPs usually have in part absorption and scattering effects, to clarify the origin of those additional photons, we compare the reflectance spectra for devices with and without Au-NPs

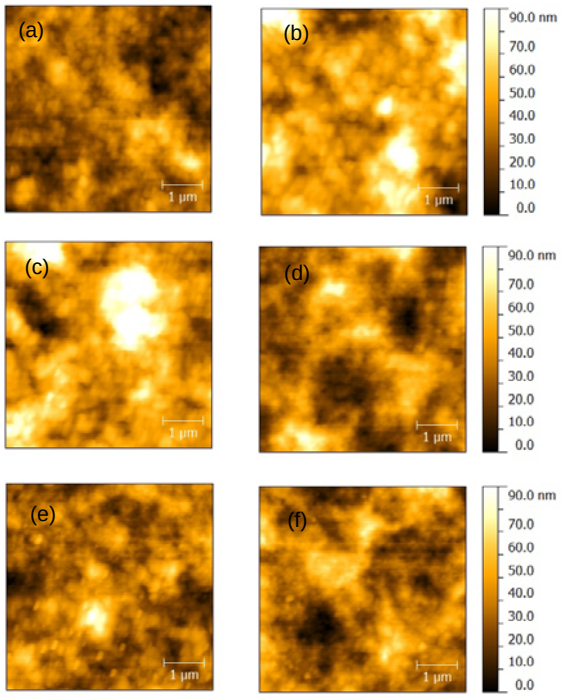

Fig. 3 Morphology image for each layer taken by atomic force microscopy (AFM). Morphologies for subsequently deposited layers on pristine ZnO-nanorod array are (a)P3HT:PCBM and (c) PEDOT:PSS (or (e) PEDOT:PSS:$Au_{20\%}$) while those depositing on 2-NT modified ZnO-nanorod arrays are (b) P3HT:PCBM, and (d)PEDOT:PSS (or (f) PEDOT:PSS:$Au_{20\%}$).

Fig. 5 (a) shows the reflectance spectra for 2-NT modified devices using PEDOT:PSS and PEDOT:PSS:$Au_{20\%}$ as the rear interlayers. The intensity of the reflectance for the device using PEDOT:PSS:$Au_{20\%}$ layer is lower than the one without Au-NP doping in the wavelengths from 400 to 650 nm. We further calculated the additional absorption, $\triangle\alpha$, from the measured reflectance spectra based on the equation $\triangle\alpha = -\ln(R_{PEDOT:PSS}/R_{PEDOT:PSS:Au20\%})$[43] to quantify the difference of absorption in the measured range, where $R_{PEDOT:PSS}$ and $R_{PEDOT:PSS:Au20\%}$ stand for the light intensity reflected from PEDOT:PSS and PEDOT:PSS:$Au_{20\%}$ rear interlayers, respectively. As can be seen in Fig. 5(b), $\triangle\alpha$ increases in the visible range of 400 – 650 nm, which indicates an additional absorption of the photoactive layer in the devices with Au-NP doped rear interlayer. Additionally, this region of enhancement coincides with that observed in the UV-vis absorption spectra for devices after incorporating Au-NPs. Since Au-NPs have in part absorption in the same spectrum region, the scattering effect of Au-NPs results in improving the light harvesting of the photoactive layer for at most 5%.

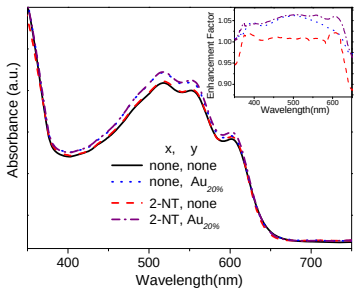

Fig 4 UV-vis spectra for cells under different manipulation conditions. The relative absorption enhancement factor for each condition is shown in the inset.

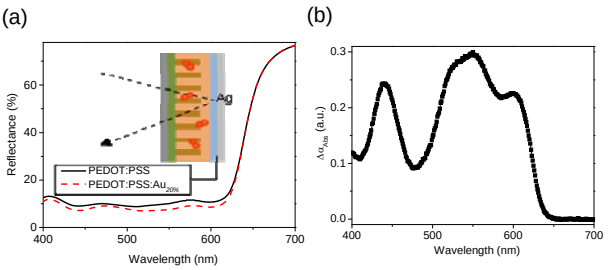

Fig. 5 (a) The reflectance spectra of 2-NT modified devices using PEDOT:PSS or PEDOT:PSS:$Au_{20\%}$ as the rear interlayer. Insect: schematic illustration of the incident light path in a completed device. (b) The additional absorption spectrum resulting from the difference of reflectance spectra between devices using PEDOT:PSS and PEDOT:PSS:$Au_{20\%}$ as the rear interlayers.

Because the photoactive layer absorbs at most 5% additional photons, it is unlikely to produce ~30% extra charge carriers for the collection as shown by the IPCE measurements. The largely enhanced J_{sc} should arise from some other factors. Based on Mihailetchi and co-workers' analytical approach,[44,45] we compared the photocurrent behavior for these cells. The photocurrent density (J_{ph}) is defined as the current density difference between the cell under illumination and in the dark, and the effective voltage (V_{eff}) is determined by $V_0 - V_a$, where V_0 is the voltage when $J_{ph} = 0$ and V_a is the applied voltage. As shown in Fig. 6(a), the J_{ph} increased linearly with V_{eff} at low voltages and then saturated at a certain high value of V_{eff}. The saturated photocurrent density (J_{sat}) is independent of the bias and temperature and can be correlated with the maximum exciton generation rate (G_{max}) through $J_{ph} = qG_{max}L$, where q is the

elementary charge and L is the thickness of the photoactive layer, by assuming that all of the photogenerated excitons are separated into free carriers and contributed to the current.[44,45] The obtained J_{sat} for (x, y) = (none, none), (none, Au$_{20\%}$), (2-NT, none), and (2-NT, Au$_{20\%}$) were 11.8, 12.8, 13.9, and 14.1 mA/cm^2, respectively, which correspond to G_{max} of 3.7 ×10^{27}, 4.0 ×10^{27}, 3.9 ×10^{27}, and 4.4 ×10^{27} m^{-3}s^{-1}, respectively. It is known that G_{max} is governed by the maximum number of photon absorbed.[42,44] The incorporation of Au-NPs in PEDOT:PSS increases G_{max}, suggests that more photons are absorbed in the photoactive layer, which is consistent with UV-vis absorbance measurement in Fig. 4. Sample treated with only 2-NT molecules also exhibits a subtle increase in G_{max}. Since the photon absorption efficiency remains the same (see Fig. 4), the enhancement can be attributed to the passivation effect of 2-NT molecules on the ZnO-nanorod surface to minimize the carrier loss at the surface defect states, such that more free charges can contribute to J_{ph}. This surface passivation effect has been resolved by the fluorescence measurement previously.[36] By taking the advantages of both treatments; i.e., LSPR and surface passivation effects, G_{max} displays the highest value among the cells.

In fact, not all the photogenerated excitons are completely dissociated into free carriers. The excition dissociation properties $P(E,T)$ can be related to J_{ph} through J_{ph} = J_{sat} $P(E,T)$.[25] The calculated $P(E,T)$ values under J_{sc} condition are 83.6%, 85.3%, 86.3%, and 87.1% for (x, y) = (none, none), (none, Au$_{20\%}$), (2-NT, none), and (2-NT, Au$_{20\%}$), respectively. Therefore, modifying either the front or the rear interlayer shows an improved exciton dissociation rate at different extent, which suggests that either SPR and 2-NT modification can effectively assist exciton separation. This role for 2-NT molecule is also evidenced by the shortening of fluorescence decay lifetime.[36] According to Wu et al.[46], LSPR enhanced exciton dissociation probability can be understood as the plasmon–exciton coupling participating in the charge transfer process and can also be further interpreted by the concept of "hot excitons," which possess excess energy to overcome their initial Coulombic potential.[47,48] With the integration of both treatments, $P(E,T)$ can be further enhanced by a factor of 4.1%. The enhancement of exciton dissociation rate can have significant contribution to the largely enhanced J_{sc}.

Open-circuit voltage decay (OCVD) technique was employed to obtain the carrier lifetime.[49] The cell was initially illuminated at a constant light intensity followed by an interruption of the illumination and the evolution of V_{oc} with time (t) was monitored simultaneously. The $V_{oc}(t)$ follows the exponential decay behavior of a specific time constant τ. By exciting the cell at different initial steady states, a set of $V_{oc}(t)$ curves can be obtained and the corresponding τ can be calculated. Fig. 6(b) displays the recorded decay transient curves of V_{oc}s under the application of a light pulse at various incident intensities for the standard sample. Using the same measurement procedures, the resulting decay lifetimes of V_{oc}s for the four types of cells along with the corresponding fits are summarized in Fig. 6(c). Based on the fitting results, one can extrapolate the carrier lifetime for each type of cell to one sun condition and the obtained values for (x, y) = (none, none), (none, Au$_{20\%}$), (2-NT, none), and (2-NT, Au$_{20\%}$) cells are 25, 67, 140, and 200 μs, respectively. The carrier lifetime for the standard cell obtained in one sun using the OCVD method has similar order of magnitude as that measured by using the impedance spectroscopy.[50] The incorporation of either Au-NPs or 2-NT molecules can effectively prolong the carrier lifetime for approximately 3 or 6-fold. By combining both approaches, the carrier lifetime can be further extended to almost 8-fold. The extension of the carrier lifetime by the inclusion of Au-NPs is a result of improved carrier mobility as suggested by Lu et al.[25] , which is also the same for the effect of 2-NT molecules as shown in Ref. 36. We have also measured the carrier mobility by employing charge extraction in a linearly increasing voltage (CELIV) method and the obtained mobility values for (none, none), (none, Au$_{20\%}$), (2-NT, none), and (2-NT, Au$_{20\%}$) are 4.0×10^{-5}, 4.6×10^{-5}, 7.5×10^{-5}, and 8.2×10^{-5} cm^{2}V^{-1}s^{-1}, respectively. There is an improvement of carrier mobility for the cells with treated interlayer and the higher mobility can reduce the probability of carrier recombination, and hence the longer carrier lifetime. Therefore, both the surface modification and LSPR effect can improve the charge transport through the active layer and interface to the electrode. The coupling effect of both approaches further maximizes the charge transport of the cell structure.

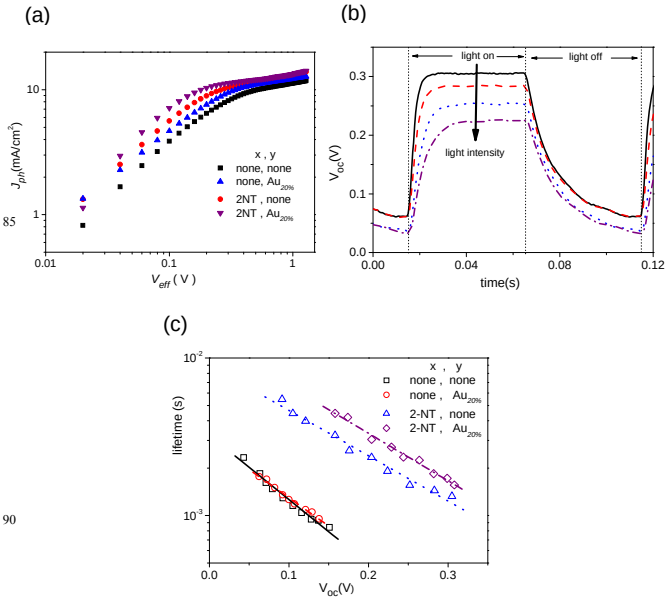

Fig. 6 (a) Photocurrent density (J_{ph}) vs. effective voltage (V_{eff}) characteristics of the standard and manipulated cells. (b) The response of open circuit voltage (V_{oc}) as a function of time to a light pulse with various light intensities. (c) The carrier lifetime as a function of V_{oc} along with a fitting curve for each type of the cell.

Based upon the above results, manipulating the dual interlayers results in a significant improvement in the performance of solar cells and the underlying mechanisms can be understood as follows. Doping the rear interlayer with Au-NPs produces at most additional 5% harvested photon numbers due to the scattering effect, which can contribute to photocurrent. Because there is no changes in V_{oc}, it suggests that the interlayer property is not altered in the presence of Au-NPs and still remains ohmic contact with Ag.[51,52] Though the series resistance (R_s) slightly increases from 5.6 ± 0.7 to 6.0 ± 0.7 Ωcm^2 and the shunt resistance (R_{sh}) subtly decreases from 274.6 ± 7.7 to 263.7

± 8.6 Ωcm^2, the cell performance is improved, revealing that the cell performance does not result from a reduction in cell resistance. Instead, there is a subtle improvement in exciton dissociation rate and carrier lifetime owing to the LSPR effect from Au-NPs. In general, an enhanced exciton dissociation probability reduces the carrier recombination rate, which is also supported by the improved carrier lifetime and, therefore, the *FF* of cells. Thus, we attribute the increased *FF* to the enhancement of exciton dissociation probability[45] and extended carrier lifetime[25] resulting from the locally enhanced electromagnetic field originating from the excitation of the LSPR. Consequently, the application of the LSPR concept can lead to an improved efficiency of the cell from 2.02 ± 0.07 % to 2.45 ± 0.13% (~21% enhancement). Modifying the front interlayer with 2-NT molecules results in ~86% enhancement in *PCE* due to largely enhanced J_{sc}, V_{oc} and *FF*. The multiple functions of 2-NT layer enhance V_{oc} due to the surface passivation effect and J_{sc} as results of improved exciton dissociation rate and a longer carrier lifetime. The higher *FF* can be partially attributed to reduced R_s from 5.6 ± 0.7 to 5.0 ± 0.7 Ωcm^2 and enhanced R_{sh} from 274.6 ± 7.7 to 294.4 ± 7.2 Ωcm^2 and partially due to the increased exciton dissociation rate and lifetime.

By integrating both approaches in a single cell, we obtain a giant enhancement in the cell performance because of taking the advantages of both treatments. Doping the rear interlayer with Au-NPs has the unique feature of benefiting the photon absorption quantity while manipulating the front interlayer is more crucial for diminishing the surface defect states of the metal-oxide layer to minimize surface recombination events. For instance, as shown in Fig. 4, the additional at most 5% harvested photons due to Au-NPs scattering produce ~30% increment in J_{sc}. The reason for this magnification effect is that, in addition to the extra absorbed photons, the carrier dynamics including both the exciton dissociation rate and the carrier lifetime are maximized through the coupling of the effects of surface modified conjugated small molecules and the LSPR. In such case, more free charges can be obtained and collected at electrodes by travelling through a better charge transport pathways. Further, the surface passivation of the front metal-oxide layer can raise the V_{oc} of the cell. Additionally, the high *FF* is attributed to the highly reduced recombination rate due to the much increased exciton dissociate probability from combining both approaches. Thus, the cell efficiency can be further maximized and a *PCE* of 4.36% for the best cell with ~ 120% increment is achieved. This sets the record of the inverted polymer solar cell using P3HT:PCBM as the photoactive layer.

Conclusion

In conclusion, a giant enhancement of inverted solar cell efficiency has been demonstrated with the integration of different approaches based on the fabrication feasibility and impact on the cell performance. The front metal-oxide interlayer adopts the surface modification strategy by self-assembled a layer of 2-NT molecules on the ZnO-nanorod surface while the rear interlayer employs the localized surface plasmon resonance effect through doping the PEDOT:PSS with Au-NPs. Particularly, the former one can effectively passivate the metal-oxide surface and the latter one can improve the photon absorption efficiency. In addition, both approaches can also effectively enhance the exciton dissociation rate and extend the carrier lifetime. With the integration of both approaches, the fabricated cell can not only take the advantages of the individual treatment, but also have the benefits of the coupling between these two approaches. Therefore, the cell efficiency can be enhanced from 2.02 % to 4.36%, which represents the highest record reported so far in inverted solar cells using ZnO-nanorod as electron transporting layer and P3HT:PCBM as the photoactive material. The proposed method can be generalized to other polymer blend systems as well and open up a new route for designing high efficiency polymer solar cells.

Acknowledgements

This work is supported by Ministry of Science and Technology, Taiwan (Project No. NSC 102 - 2112 - M - 239 - 001 - MY3).

Notes and references

[a] *Department of Physics, National Taiwan University, Taipei 106, Taiwan. Email: yfchen@phys.ntu.edu.tw (Y. F. Chen)*
[b] *Institute of Electro-Optical Science and Technology, National Taiwan Normal University, Taipei 106, Taiwan*
[c]*Department of Materials Science and Engineering, National United University, Miaoli 360, Taiwan. Email: fangchi@nuu.edu.tw*

1 F. C. Krebs, S. A. Gevorgyan, and J. Alstrup, J. of Mater. Chem. 2009, **19**, 5442.
2 T. D. Nielsen, C. Cruickshank, S. Foged, J. Thorsen, and F. C. Krebs, Sol. Energy Mater. Sol. Cells 2010, **94**, 1553.
3 G. Li, R. Zhu, and Y. Yang, Nat. Photon., 2012, **6**, 153.
4 C .-Z. Li, H. -L. Yip, and A. K. -Y. Je, 2012, **22**, 4161–4177.5 T. J. Savenije, J. M. Warman, and A. Goossens, Chem. Phys. Lett. 1998, **287**, 148.
5 C. E. Small, S. Chen, J. Subbiah, C. M. Amb, S. W. Tsang, T. H. Lai, J. R. Reynolds, and F. So, Nat. Photon. 2012, **6**, 115.
6 L. T. Dou, J. Gao, E. Richard, J. B. You, C. C. Chen, K. C. Cha, Y. J. He, G. Li, and Y. Yang, J. of Am. Chem. Soc. 2012, **134**, 10071.
7 Y. F. Li, Accounts Chem. Res. 2012, **45(5)**, 723 .
8 P. M. Beaujuge, and J. M. J. Fréchet, J. Am. Chem. Soc. 2011, **133**, 20009.
9 F. He, and L. P. Yu, J. Am. Chem. Soc. Lett. 2111, **2** 3102.
10 G. Li, C. W. Chu, V. Shrotriya, J. Huang, and Y. Yang, Appl. Phys. Lett. 2006, **88**, 253503.
11 C. Tao, S. Ruan, X. Zhang, G. Xie, L. Shen, X. Kong, W. Dong, C. Liu, and W. Chen, Appl. Phys. Lett. 2008, **93**, 193307.
12 C. Waldauf, M. Morana, P. Denk, P. Schilinsky, K. Coakley, S. A. Choulis, and C. J. Brabec, Appl. Phys. Lett. 2006, **89**, 233517.
13 Z. Tan, L. Li, F. Wang, Q. Xu, S. Li, G. Sun, X. Tu, X. Hou, J.Hou, and Y. Li, Adv. Energy Mater. 2014, **4**, 1300884.
14 M.S. White, D.C. Olson, S.E. Shaheen, N. Kopidakis, and D.S. Ginley, Appl. Phys. Lett. 2006, **89**, 143517.
15 F. Liu, Z.A. Page, V. V. Duzhko, T. P. Russell, and T. Emrick, Adv. Mater. 2013, **25**, 6868.
16 Y. Zhou, F. Li, S. Barrau, W. Tian, O. Inganas, F.L. Zhang, Sol. Energy Mater. Sol. Cells 2010, **94**, 497.
17 S. I. Na, T.S. Kim, S.H. Oh, J. Kim, S.S. Kim, and D.Y. Kim, Appl. Phys. Lett. 2010, 97, 223305.
18 L. Motiei, Y. Yao, J. Choudhury, H. Yan, T. J. Marks, M. E. van der Boom, and A. Facchetti, J. Am. Chem. Soc. 2010, **132**, 12528.
19 Y. Yuan, T.J. Reece, P. Sharma, S. Poddar, S. Ducharme, A. Gruverman, Y. Yang, and J.S. Huang, Nat. Mater.2011, **10**, 296.
20 Y. Zhu, X. Xu, L. Zhang, J. Chen, and Y. Cao, Sol. Energy Mater. Sol. Cells 2012, **97**, 83.

21 Z. Tan, L. Li, C. Li, L. Yan, F. Wang, J. Xu, L. Yu, B. Song, J. Hou and Y. Li, Adv. Mater. Interfaces DOI: 10.1002/admi.201400197.

22 Z. Tan, S. Li, F. Wang, D. Qian, J. Lin, J. Hou, and Y. Li, Sci. Rep. 2014, **4**, 4691.

23 Z. Tan, W. Zhang, Z, Zhang, D. Qian, Y. Huang, J. Hou, and Y. Li, Adv. Mater. 2012, **24**, 1476.

24 F.-C. Chen, J.-L. Wu, C.-L. Lee, Y. Hong, C.-H. Kuo, and M. H. Huang, Appl. Phys. Lett. 2009, 95, 013305.

25 L. Lu, Z. Luo, T. Xu, and L. Yu, Nano Lett. 2013, **13**, 59.

26 X. Yang, C.-C. Chueh, C.-Z. Li, H.-L. Yip, P. Yin, H. Chen, W.-C. Chen, and A. K-Y. Jen, Adv. Energy Mater. 2013, **3**, 666.

27 R. Thitima, C. Patcharee, S. Takashi, and Y. Susumu, Solid State Electron. 2009, **53**, 176.

28 X. Bulliard, S. G. Ihn, S. Yun, Y. Kim, D. Choi, J. Y. Choi, M. Kim, M. Sim, J. H. Park, W. Choi, and K. Cho, Adv. Funct. Mater. 2010, **20**, 4381.

29 Y. M. Sung, F. C. Hsu, and Y. F. Chen, Sol. Energy Mater. Sol. Cells 2014, **125**, 239.

30 Y. Y. Lin, Y. Y. Lee, L. Chang, J. J. Wu, and C. C. Chen, Appl. Phys. Lett. 2009, **94**, 063308.

31 C. T. Chen, F.C. Hsu, Y.M. Sung, H. C. Liao, W. C. Yen, W. F. Su and Y. F. Chen, Sol. Energy Mater. Sol. Cells 2011, **95**, 740.

32 J. Y. Chen, F.C. Hsu, Y.M. Sung, and Y. F. Chen, J. Mater. Chem. 2012, **22**, 15726.

33 T. C. Monson, M. T. Lloyd, D. C. Olson, Y. J. Lee, and J. W. P. Hsu, Adv. Mater. 2008, **20**, 4755.

34 C. Goh, S. R. Scully, and M. D. McGehee, J. Appl. Phys. 2007, **101**, 114503.

35 J. Yu, T. L. Shen, W. H. Weng, Y. C. Huang, C. I. Huang, W. F. Su, S. P. Rwei, K. C. Ho, and L. Wang, Adv. Energy Mater. 2012, **2**, 245.

36 J.Y. Chen, F.C. Hsu, Y.M. Sung, and Y. F. Chen, J. Mater. Chem. 2011, **22**, 15726.

37 L. Vayssieres, Adv. Mater. 2003, **15**, 464.

38 J. Singh, J. Im, J.E. Whitten, J.W. Soares, and D.M. Steeves, Langmuir 2009, **25**, 9947.

39 D.C. Lim, K.-D. Kim, S.Y. Park, E.M. Hong, H.O. Seo, J.H. Lim, K.H. Lee, Y. Jeong, C. Song, E. Lee, Y. D. Kim, and S. Cho, Energy Environ. Sci. 2012, **5**, 9803.

40 D. C. Olson, J. Piris, R. T. Collins, S. E. Shaheen, and D. S. Ginley, Thin Solid Films., 2006, **496**, 26.

41 Y. M. Sung, F. C. Hsu, D. Y. Wang, I. S. Wang, C. C. Chen, H. C. Liao, W. F. Su, and Y. F. Chen, J. Mater. Chem. 2011, **21**, 17462.

42 C. J. Barbec, N. S. Sariciftci, and J. C. Hummelen, Adv. Funct. Mater.2011, **11**, 15.

43 J. Y. Kim, S. H. Kim, H. H. Lee, K. Lee, W. L. Ma, X. Gong, A. J. Heeger, Adv. Mater. 2006, **15**, 572.

44 V. D. Mihailetchi, L. J. A. Koster, J. C. Hummelen, and P. W. M. Blom, Phys. Rev. Lett. 2004, **93**, 216601.

45 V. D. Mihailetchi, H. X. Xie, B. de Boer, L. J. A. Koster, and P. W. M. Blom, Adv. Funct. Mater. 2006, **16**, 699.

46 J. L. Wu, F. C. Chen, Y. S. Hsiao, F. C. Chien, P. L. Chen, C. H. Kuo, M. H. Huang, and C. S. Hsu, ACS Nano., 2011, **5**, 959.

47 J. H. Lee, J. H. Park, J. S. Kim, D. Y. Lee, K. Cho, Org. Electron. 2009, **10**, 416.

48 H. Ohkita, S. Cook, Y. Astuti, W. Duffy, S. Tiemey, W. Zhang, M. Heeney, I. McCulloch, J. Nelson, D. D. C. Bradley, and J. R. Durrent, J. Am. Chem. Soc. 2008, **130**, 3030.

49 A. Zaban, M. Greenshtein, and J. Bisquert, Chem. Phys. Chem. 2003, **4**, 859.

50 G. Garcia-Belmonte, P. P. Boix, J. Bisquert, M. Sessolo, and H. J. Bolink, Sol. Energy Mater. Sol. Cells 2010, **94**, 366.

51 T. Z. Oo, N. Mathews, G. C. Xing, B. Wu, B. G. Xing, L. H. Wong, T. C. Sum, S. G. Mhaisalkar, J. Phys. Chem. C., 2012, **116**, 6453.

52 M. Heo, H. Cho, J. W. Jung, J. R. Jeong, S. Park, J. Y. Kim, Adv. Mater. 2011, **23**, 5689.